






Please cite the Published Version

Hoque, Abdullah Mohammad Tanvirul , Altabatabaie, Kusay Faisal , Habib, Md Ahasan , Ahsan, Mominul  and Haider, Julfikar  (2024) Titanium-Coated Extremely Sensitive SPR Biosensor for Cancer Cell Detection. *Journal of Sensors*, 2024. 4748809 ISSN 1687-7268

DOI: <https://doi.org/10.1155/2024/4748809>

Publisher: Wiley

Version: Published Version

Downloaded from: <https://e-space.mmu.ac.uk/636452/>

Usage rights:  [Creative Commons: Attribution 4.0](https://creativecommons.org/licenses/by/4.0/)

Additional Information: ** From Hindawi via Jisc Publications Router ** History: publication-year 01-01-2024; received 27-03-2024; rev-recd 05-08-2024; accepted 30-08-2024; archival-date 15-10-2024; ppub 15-10-2024. ** Licence for this article: <https://creativecommons.org/licenses/by/4.0/>

Data Access Statement: The data presented in this study are available in the article.

Enquiries:

If you have questions about this document, contact openresearch@mmu.ac.uk. Please include the URL of the record in e-space. If you believe that your, or a third party's rights have been compromised through this document please see our Take Down policy (available from <https://www.mmu.ac.uk/library/using-the-library/policies-and-guidelines>)

Research Article

Titanium-Coated Extremely Sensitive SPR Biosensor for Cancer Cell Detection

Abdullah Mohammad Tanvirul Hoque ¹, Kusay Faisal Altabatabaie ²,
Md. Ahasan Habib ³, Mominul Ahsan ⁴ and Julfikar Haider ⁵

¹Wyant College of Optical Sciences, The University of Arizona, Tucson, USA

²Department of Computer Science, Cihan University Sulaimaniya, Sulaimaniya, Iraq

³Department of Electrical and Electronic Engineering, Rajshahi University of Engineering and Technology, Kazla, Rajshahi 6204, Bangladesh

⁴Department of Computer Science, University of York, Deramore Lane, York, YO10 5GH, UK

⁵Department of Engineering, Manchester Metropolitan University, Chester Street, Manchester, M1 5GD, UK

Correspondence should be addressed to Mominul Ahsan; mominul.ahsan@york.ac.uk

Received 27 March 2024; Revised 5 August 2024; Accepted 30 August 2024

Academic Editor: Arun Uniyal

Copyright © 2024 Abdullah Mohammad Tanvirul Hoque et al. This is an open access article distributed under the Creative Commons Attribution License, which permits unrestricted use, distribution, and reproduction in any medium, provided the original work is properly cited.

In this study, a D-shaped, extremely sensitive surface plasmon resonance (SPR) sensor with a blue shift characteristic is proposed that can be used to identify various malignant cancer cells. A sensing layer made of titanium is inserted to produce intense sensitivity. For the simulation and numerical evaluation of the proposed biosensor, we used the finite element method (FEM) and the COMSOL Multiphysics 5.6 software. To regulate how much light passes through the sensor, which incites the released electrons at the surface of the plasmonic material, air holes in different radii are used. The characteristics that make our proposed sensor superior to other D-shaped SPR sensors are—it gives an excellent amplitude sensitivity (AS) of 200 RIU^{-1} also ensures extremely high wavelength sensitivity (WS) spanning from 34,350 to 42,145 nm/RIU with an outstanding spectral resolution of 2.37×10^{-6} RIU. Furthermore, the R^2 (0.9966) value is also extremely close to 1 which ensures the quality of our sensor regarding its performance. The given sensor is tailored for four vital human cancers, which are blood cancer, skin cancer, cervical cancer, and adrenal gland cancer. Here, optimization of the structural geometric parameters, plasmonic materials, and material thickness are also conducted in search of the best functionality of the sensor. The offered structure, nonetheless, can be an obvious prologue in the case of the crucial human cancer detection platform due to its mild sensing performances.

Keywords: biosensor; cancer cell; COMSOL Multiphysics; detection; FEM; FOM; PCF; SPR; wavelength sensitivity

1. Introduction

Cancer is ranked as the second leading cause of human mortality globally [1]. The World Health Organization (WHO) estimates that cancer kills 1 in 6 people worldwide [2], and there would be roughly 19.3 million new cases and 10 million deaths from cancer by the year 2020 [3]. As a consequence of early cancer identification, the likelihood of a patient's survival is increased [4]. The most common methods of identifying cancer are biopsies, physical examinations, endoscopic procedures, and imaging, including X-rays and MRI

(magnetic resonance imaging). However, these solutions require a substantial financial commitment and pricey diagnostic setups [4]. Therefore, a rapid, effective, and precise clinical diagnostic technique for cancer diagnosis is essential. Due to severe potential in sensing applications, the surface plasmon resonance (SPR)-based sensing technique has received a lot of interest [5]. Prism-based SPR sensor was previously employed where the prism was covered with a plasmonic material. In a specific incident angle, the incident light frequency and the frequency of the released electron coincide, resulting in a surface plasmon wave with a metallic-dielectric interface [6].

However, owing to the optical and mechanical equipment, prism-based SPR sensors are architecturally large and bulky, making them unsuitable for distant sensing [7]. However, this problem can be solved by using an SPR-based photonic crystal fiber (PCF) sensor because SPR-PCF sensors are miniaturized in size, relatively inexpensive, consume lower power, and have extremely narrow resonance properties with extreme sensitivity. Moreover, it gives a label-free detection system that can decrease the perplexity of the test [4], better light confinement, propagation control of light, birefringence properties, etc. [8]. Also, PCF sensors are superior to prism-based and fiber-based sensors are higher integration potential, wider range applications, enhanced multiplexing that allows us for simultaneous detection of multisamples, the microstructured design of PCFs provides better control over light propagation and reduced optical losses, etc.

SPR-PCF sensor is frequently employed in environmental monitoring, disease identification, chemical detection, and other applications and can only be lighted in general events with the use of broadband light sources [4, 9]. Various technologies such as microfluid [10], electronic chemicals [11], immunological chemistry [12], and molecular-level cancer diagnosis [13] have become more common day by day. In 1985, Clark [14] launched the first SPR biosensors for testing the glucose level in blood testing. Yaroslavsky et al. hypothesized the identification of a carcinoma cancer [15], the influence of luminous-thermal on the nano-synthesis structure [16], and cancer appears in bodily fluids after the events of various locations [17, 18]. Wu et al. [19] reviewed advancements in single mode–multimode–single mode (SMS) fiber structures for sensing applications, discussing mechanisms for refractive index (RI), temperature, strain, and curvature sensing. Challenges include improving robustness in harsh environments, enhancing signal stability, and developing cost-effective fabrication techniques. Chen et al. [20] developed an ultrahigh-sensitivity, label-free optical fiber biosensor using a tapered single mode-no core-single mode (SNS) coupler to detect *Staphylococcus aureus*. The study focuses on sensitivity but lacks a detailed discussion on specificity, cross-reactivity, long-term stability, reusability, and scalability of the fabrication process. Kumar et al. [21] created an ultrasensitive biosensor (detection limit [DL] is 0.0001 mIU/mL) using a microfiber interferometer enhanced with magnetic microspheres, validated for detecting low concentrations of target analytes. The paper emphasizes sensitivity but does not thoroughly address specificity, selectivity, or integration into existing diagnostic systems. Salah, Pal, and Uniyal [22] proposed a method of enhancing SPR-based sensors' sensitivity (the highest sensitivity is 3269.4 nm/RIU) and accuracy through wavelength interrogation to detect fuel adulteration by changes in RI. However, environmental factors like temperature and pressure could affect their reliability in real-world applications. Bijalwan et al. [23] developed a temperature sensor (highest sensitivity was 0.249 deg/°C) using E7 liquid crystals with SPR technology and angle interrogation for improved sensitivity and accuracy. The sensor design, however, is complex and requires specialized equipment and expertise. Almagwani et al. [24] created an SPR sensor (sensitivity and figure of

merits (FOM) were 253.68 deg/RIU and 43.30 RIU⁻¹) enhanced with magnesium oxide (MgO) and silicon (Si) for gas detection, validated under various conditions. Challenges include material compatibility and stability, which may impact durability and performance consistency. Pal et al. [25] designed a long-range SPR biosensor for hemoglobin detection, validated through experiments with human blood samples. While optimized for hemoglobin, it may struggle with specificity, potentially confusing it with similar proteins or compounds. Karki et al. [26] developed an SPR gas sensor using multilayer black phosphorus (BP), exploring how layer variations affect sensitivity (the maximum sensitivity and FOM were 374.31/RIU and 37.63 RIU⁻¹). Both theoretical and experimental validations were conducted, but the complexity of controlling the layers may hinder reproducibility. Hemanth et al. suggested a 2D photonic crystal-based cervical cancer sensor (simulation-based) that gives the highest sensitivity of 143 nm/RIU [27]. Karki et al. [28] developed an RI sensor structure incorporating layers of platinum diselenide and graphene, which are indicative of the presence of cancer biomarkers (maximum sensitivity and FOM are 235°/RIU and 41.14 RIU⁻¹). However, the integration of PtSe2 and graphene layers might present significant fabrication challenges. Karki et al. [29] have provided a comprehensive review of the recent advancements in SPR-based biosensor technologies specifically for cancer cell detection. The authors highlighted different applications of SPR biosensors in the detection of various types of cancer cells. They have discussed various techniques and approaches used to enhance the sensitivity and specificity of SPR biosensors. Karki et al. [30] developed a SPR biosensor incorporating zinc sulfide (ZnS), silicon dioxide (SiO₂), and BP to enhance sensitivity. They have conducted experiments to test the biosensor's sensitivity and compared it with other SPR biosensors. Karki et al. [31] developed an SPR sensor that integrates ZnO and Si to enhance the sensitivity and performance of the sensor. The authors have conducted experiments to evaluate the sensor's sensitivity to various chemical compounds (the highest sensitivity is 311°/RIU, which was obtained for 1.36 [Acetone]). Karki et al. [32] explore the application of transition metal dichalcogenides (TMDCs) in enhancing SPR sensors for detecting fat concentration in milk. They have conducted experiments to measure the sensor's response to varying fat concentrations in milk samples (the highest sensitivity, detection accuracy, and FOM are 314°/RIU, 0.142/°, and 44.05/RIU, respectively). However, integrating TMDCs into SPR sensors could complicate the manufacturing process. Karki et al. [33] have designed and fabricated an SPR sensor using a combination of gold, MXene, and graphene nanofilms. They have integrated MXene and graphene to enhance the sensor's sensitivity and specificity (the maximum sensitivity is 258.28°/RIU). Karki et al. [34] introduced a sensor capable of detecting glucose concentration in urine samples, achieving a sensitivity down to 0.15 mg/dL. They designed and evaluated a highly sensitive SPR sensor using the Kretschmann configuration. Their study highlighted that incorporating MXene, ZnO, and graphene layers enhanced angular sensitivity. Hoque et al. [35] proposed a dual-polarized

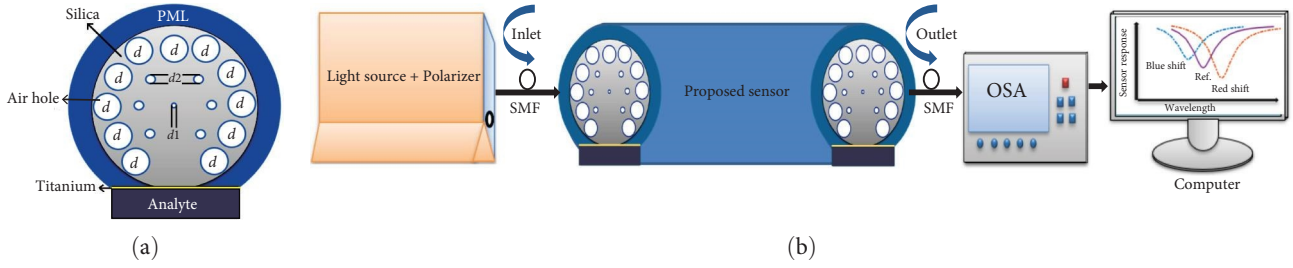


FIGURE 1: (a) The transverse sectional sight of the presented sensor and (b) the experimental setup diagram. OSA, optical spectrum analyzer; PML, perfectly matched layer; SMF, single-mode fiber.

circular-shaped single analyte SPR sensor (simulation-based), which demonstrated the highest wavelength sensitivity (WS) of 13,700 and 15,400 nm/RIU for x and y polarized mode successively. Jabin et al. [36] developed (simulation-based) a D-shaped breast cancer sensor with a peak sensitivity level of 18,000 nm/RIU. The majority of previously suggested cancer sensors relied solely on Basal cells, measured sensitivity with another malignant cell characteristic, and had a sensitivity threshold of less than 18,000 nm/RIU [36].

In this study, a unique PCF design has been proposed to provide even greater versatility and sensitivity for the quick detection of many kinds of malignant cells, such as skin cancer cells (Basal), blood cancer cells (Jurkat), cervical cancer cells (HeLa), and adrenal glands cancer cells (PC12). A D-shaped structure is proposed that exhibits blue shift characteristics making it an exceptional sensor, with a thin titanium (Ti) layer (40 nm) placed between the silica and the cancer cell to provide exceptional wavelength and amplitude sensitivity (AS). The maximum wavelength and AS of this suggested sensor are 42,145 nm/RIU and 200 RIU⁻¹, respectively. The detection performance was assessed by the finite element method (FEM), and all the sensitivity characteristics of different types of malignant cells were compared to their normal counterparts. The use of the FEM ensures promising detection performance parameters for the SPR biosensor by precisely modeling complex sensor structures, accurately simulating electromagnetic fields, optimizing design parameters for maximum sensitivity, and incorporating material properties accurately, etc. However, it can help in early cancer detection by identifying the cancer bio-markers when present in low concentrations, thus facilitating the timely initiation of therapy. Also, it can detect microbial infections, which is crucial for fast and proper medical intervention through the determination of pathogens and their antibiotic resistance. Additionally, it can contribute to Healthcare Diagnostics by detecting changes in certain biological markers, disease progression can be monitored as well as the establishment of treatment efficacy.

2. Sensor Modeling and Theoretical Analysis

The cross-sectional sight of the suggested D-shaped model with mono-core transmission mode is displayed in Figure 1a. To set up the centrally regulated transmission, we used scaled-down (SCD) air holes (AHs), Si, and perfectly matched layer (PML) are employed as the background materials in our proposed D-shaped sensor. The interior lattice arrangement

in the core area is enclosed by a ring structure made up of a series of AHs. In the bottom part of the structure, a rectangular-shaped analyte layer (AL) is deposited, and a thin Ti layer (40 nm) is placed above it. The sensitivity to bio-samples can be influenced by changes in AHs, and fiber cladding will be formed by larger internal perforated capillaries. The cladding layer maintains the proper degree of light restriction by modifying the whole internal reflection at the air-silica contact.

The pitch (Λ) of the PCF is defined as the central-to-central space between the two adjacent capillaries. To ensure the best detection performance, each structural parameter of the sensor was individually optimized and finalized by using trial and error method, including $\Lambda = 1.9 \mu\text{m}$, large AH diameter (AHD) (d) = 0.9 μm , small AHD (d_2) = 0.5 μm , smallest AHD (d_1) = 0.2 μm , liquid layer = 1.2 μm , and PML = 1.06 μm . The RI of the fused silica material can be evaluated by using the following Sellmeyer equation [37].

$$n^2 = 1 + \frac{B_1 \lambda^2}{\lambda^2 - C_1} + \frac{B_2 \lambda^2}{\lambda^2 - C_2} + \frac{B_3 \lambda^2}{\lambda^2 - C_3}, \quad (1)$$

where the effective RI of fused silica is denoted by n , and the values of all mentioned constants for fused silica ($B_1, B_2, B_3, C_1, C_2,$ and C_3) known as Sell Meier's constants have been taken from the paper [35]. We used Ti as the plasmonic material in our proposed sensor due to some of its advantages, which are as follows: it is more biocompatible and cheaper than gold or silver, and it exhibits excellent chemical stability (more resistant to corrosion). Furthermore, it is lightweight and its high mechanical strength allows us for robust sensor construction. However, it has lower plasmonic performance than gold or silver and achieving a smooth Ti surface necessary for optimal plasmonic performance can be challenging due to surface roughness. The deposited metal (Ti) film has an intensive impact on the sensing performance of the SPR-PCF sensor. The relative complex dielectric constant of Ti film is computed by using the following Drude-Lorentz model [38]:

$$\epsilon_{Ti} = \epsilon_\infty - \frac{(\hbar\omega_p)^2}{E^2 + (\hbar\Gamma)E} + \sum_{j=1}^n \frac{A_j E_j^2}{E_j^2 - E^2 - iBr_j E}, \quad (2)$$

where ϵ_∞ is the dielectric constant at high frequency set to unity, $\hbar\omega_p$ and $\hbar\Gamma$ represent the Drude parameters for

TABLE 1: RI information of different cancerous and normal cells.

Type of cancer	Cell name	RI
Blood cancer	Jurkat cell	1.390
	Normal cell	1.376
Skin cancer	Basal cell	1.380
	Normal cell	1.360
Cervical cancer	HeLa cell	1.392
	Normal cell	1.368
Adrenal glands cancer	PC12 cell	1.395
	Normal cell	1.381

Abbreviation: RI, refractive index.

unscreened plasma frequency (E_p) and free-carrier damping (E_f), respectively. In addition, A_j , E_j , and Br_j describe the Lorentzian oscillator, denoting the amplitude, energy, and broadening of the j th absorption band, respectively.

The transverse sectional view of the experimental set-up is displayed in Figure 1b, where a broadband light source is used that can conduct optical energy into the usual single-mode fiber (SMF) [39]. Both the inlet and outlet syringe can be used to conduct the analyte through the pump. We know that the characteristics of light, like its speed, depend on the medium it is passing through due to the different RI values of the different mediums. Similarly, due to having distinguished internal protein structures of different types of cancer viruses, they have separate RIs, and therefore, we have separate outputs, particularly the different SPR points, which can be either blue shift or red shift characterized. However, by using the optical spectrum analyzer (OSA) or photodetector that can be weighed without difficulties. The sensitivity differences of each cancer cell can be assessed for their nonaffected cells. The RI of Basal, Jurkat, HeLa, and PC12 cancer cells and their corresponding normal cell ranges are shown in Table 1 [36, 40]. Our proposed model shows promising performance, offering optimized sensitivity for the rapid detection of cancer from cell liquid at an 80% concentration in comparison to normal cells at concentrations ranging from 30% to 70%.

In this model, the AL and plasmonic material layer are externally deposited on the flat segment of the D-shaped sensor, providing higher stability and visibility performance as the gap between the fiber core and the metal layer allows the entire radius of the core to be used, which results in increased plasmonic. Furthermore, the externally coated sensor is easy to coat uniformly due to outside coating and relatively lower losses than the internal sensing method. However, the D-fashioned SPR-PCF sensor indicates promise for virus detection due to its excessive sensitivity and specificity. But sensible challenges encompass sensitivity to environmental factors like temperature, and problems in the appropriate fabrication of the sensor. The temperature has a significant impact on SPR sensors like RI can be changed even the structure parameters (for example, the thickness of the metal layer). Furthermore, in complex organic fluids, there can be interference from proteins and other biomolecules. To cope with these issues, we must maintain a temperature-stable environment to mitigate this issue, and we may use

something like a thermoelectric cooler or heater around the SPR sensor in real-time applications. Additionally, future work will be cognizance on incorporating compensation mechanisms, enhancing fabrication techniques, and enhancing specificity with selective binding retailers. Regardless of these challenges, the sensor's ability for early-stage virus detection remains tremendous. In this paper, commercially available simulation software is used to conduct the FEM-based analysis (COMSOL Multiphysics 5.5), which has a pretty-high mesh size (integrated) of 28,824 subdomains bordered by 2437 boundaries, which allows us to get precise model information.

3. Results and Discussion

The prime purpose of the presented sensor is to identify the different types of human cancer by FEM method investigations and the overall change in the light absorption by the selected analytes. Any plasmonic model encounters an inalterable issue with losses of phase captivity. Typically, propagation loss is utilized to the meaning of the sensitivity of any plasmonic design that can be measured by using the following equation [41].

$$\alpha(\text{dB/cm}) = 8.686 \times k_0 \times I_m(n_{\text{eff}}) \times 10^4, \quad (3)$$

where $k_0 = 2\pi/\lambda$ indicates the number of waves in free space, $I_m(n_{\text{eff}})$ is denoted for the imaginary portion of the analyte RI, and λ indicates the wavelength. The electric field distributions of the desired modes show the paths of excitation and leakage intensity of the modeled sensor. The energy transferring is the sensing technique of the SPR sensor and at a certain wavelength, the highest absorption is estimated. The PML is an outlying circle of the structure, which is utilized to prevent and absorb the reflection of the straying energy and bright energy from the fiber axis. Figure 2 visualizes the electric fields distribution for the core mode and surface plasmon polariton (SPP) mode of cancerous cells (for RI 1.39, Figure 2a,b) and corresponding normal cell (for RI 1.376, Figure 2c,d), respectively, for y -polarization. The light is amply demonstrated to be strongly constrained at the core in the core mode, while the SPR mechanism causes the SPP mode to rebuild the resonance at the surface [42]. The free electrons on a metal surface are excited by the electromagnetic field that leaks during light propagation. Figure 3a illustrates the dispersion concern between the core mode and SPP mode of the sensor for y -polarization, which is known as the phase matching technique. In the SPR-PCF sensors, these two modes are introduced to yield the effect of SPR when the phase-matching state is found. At the intersection point (at 1887 nm), SPR takes place and transfers the most energy from core-guided mode to SPP mode as the free electrons' frequency and the electromagnetic field's leaky frequency coincide [35, 43]. In the plot, the real (n_{eff}) of the core mode and the SPP mode are pictured by the light-brown and deep-brown dash line, respectively. In Figure 3b, the birefringence characteristic curve for the analyte RI of 1.39 is displayed. The differences between the real part of the effective indices of x and y polarization modes are known as

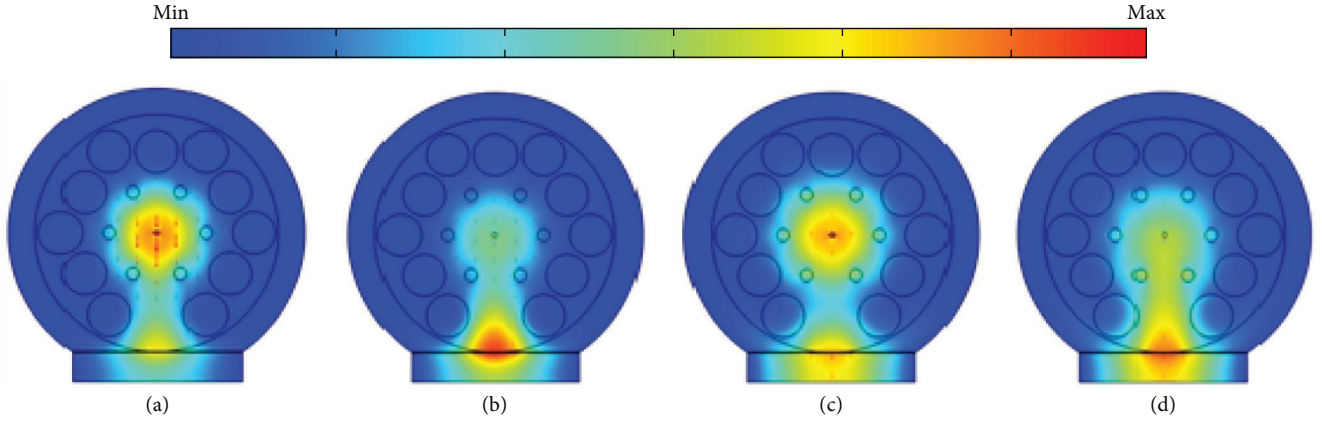


FIGURE 2: The ordination of the electric field in the sensor's core-guided mode and SPP mode at analyte RI 1.39 (a, b) and 1.376 (c, d), respectively, for the y -polarized mode. RI, refractive index; SPP, surface plasmon polariton.

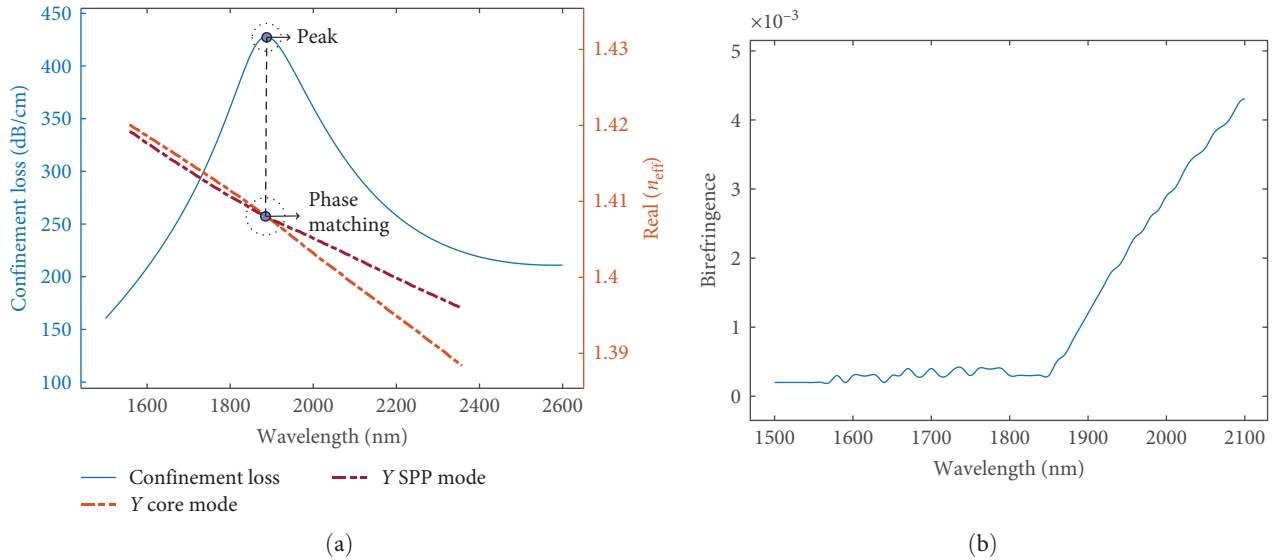


FIGURE 3: (a) Phase-matching visualization for y -polarized mode and (b) birefringence response of the structure at analyte RI of 1.39. RI, refractive index; SPP, surface plasmon polariton.

birefringence, which may help to avoid the risk of false-positive feedback. In addition, high birefringence helps to maintain the polarization state of the input signal and enhances the overall stability of the optical operation [44]. The birefringence of the proposed D-shaped SPR sensor can be evaluated by the following equation [40, 45].

$$B = |n_x - n_y|, \quad (4)$$

where n_x and n_y indicate the real part of the effective indices for x and y polarized modes correspondingly. A strong birefringent response of 9.42×10^{-4} is denoted at the resonant wavelength, which indicates there is a severe polarity difference between x and y polarization modes. The coupling length can be defined as the least value of length that allows a maximum amount of light to pass through the small cores in fused silica. The coupling-length L_c for the D-shaped SPR sensor can be evaluated by [40, 45].

$$L_c = \frac{\lambda}{2|n_x^i - n_y^i|}. \quad (5)$$

The highest coupling length exhibited by the sensor is 9,435,000 nm (Table 2). The most significant parameters of the PCF-SPR sensor are WS and AS, which are taken into consideration to define the sensitivity of the plasmonic sensor. In general, the WS displays a higher sensitivity response than amplitude interrogation although the wavelength interrogation process and its application criteria are comparatively more expensive than the AS technique as the WS process needs the whole spectra of the signal. However, WS means wavelength shifting of peak points of different cancer cells regarding their corresponding normal cells and it can be measured by applying the subsequent equation [46].

$$S_\lambda (\text{nm}/\text{RIU}) = \frac{\Delta \lambda_{\text{peak}}}{\Delta n_a}, \quad (6)$$

TABLE 2: The performance table of the proposed sensor.

Analyte RI	Res. wave. (nm)	Res. shift (nm)	Peak loss (dB/cm)	Wave. sens. (nm/RIU)	Ampl. sens. (RIU ⁻¹)	FWHM (nm)	FOM (RIU ⁻¹)	Coupling length (nm)	Wave. res. (RIU)	DL (RIU ² /nm)
1.38	2322	687	644	34,350	73	598	58	967,500	3.00×10^{-6}	7.0×10^{-11}
1.36	3009	N/A	725	N/A	N/A	N/A	N/A	716,429	N/A	N/A
1.39	1887	590	427	42,145	147	860	50	9,435,000	2.37×10^{-6}	5.7×10^{-11}
1.376	2477	N/A	651	N/A	N/A	N/A	N/A	825,667	N/A	N/A
1.392	1830	925	328	38,541	100	1145	33	9,150,000	2.70×10^{-6}	6.3×10^{-11}
1.368	2755	N/A	683	N/A	N/A	N/A	N/A	765,278	N/A	N/A
1.395	1767	515	230	36,786	200	1545	23	8,835,000	2.80×10^{-6}	6.6×10^{-11}
1.381	2282	N/A	644	N/A	N/A	N/A	N/A	950,833	N/A	N/A

Abbreviations: DL, detection limit; FWHM, full-width-half-maxima; RI, refractive index.

where Δn_a denotes the difference of analyte RI, and $\Delta \lambda_{\text{peak}}$ indicates the shifting of the wavelength peak. The broad operating wavelength range of the proposed sensor is 700–3200 nm, and the appeal of selecting a broad operating wavelength band for SPR-PCF sensor applications is that it can enhance the sensor's versatility, optimize its performance under varied conditions, allow diverse analytes to be supported, and enable ongoing R&D in optical sensing technologies while making the device more future-proof against changing sensing needs, etc. As we stated before, AS is another indicative parameter of the sensor performance, which is cost-efficient due to the unneeded spectral interpolation at a given frequency. The AS can be calculated by applying the subsequent equation [46].

$$S_A(\text{RIU}^{-1}) = -\frac{1}{\alpha(\lambda_{n_a})} \frac{\delta(\lambda_{n_a})}{\delta n_a}, \quad (7)$$

where $\alpha(\lambda, n_a)$ indicates the loss depth of the sample RI, moreover $\partial \alpha(\lambda, n_a)$ denotes the distinction between the two loss curves. Another significant sensor's numerical factor is resolution, which points out the lowest variation in analyte RI that can change the detection capability. Sensor resolution is related to measurement and accuracy, although there is no similarity between them. The sensor's precision may be significantly less expected as compared to its resolution. It can be calculated by the following equation [46].

$$R(\text{RIU}) = \Delta n_a \times \frac{\Delta \lambda_{\text{min}}}{\Delta \lambda_{\text{peak}}}. \quad (8)$$

Here, the minimum spectral resolution λ_{min} is assumed as 0.1 nm [35]. Figure 4 shows the loss curves and AS curves for different cancerous cell and their corresponding normal cell for y -polarized mode. Due to the blue shift characteristic of the proposed sensor, the resonant wavelengths for different analytes move gradually toward the vertical extent of wavelength with respect to the decrease of analyte RI. In Figure 4a, the confinement losses and AS curves for blood cancerous cell (Jurkat) and its respective normal are displayed, which displays the peak confinement losses of 427 and 651 dB/cm at 1887 and 2477 nm, correspondingly.

Similarly, in Figure 4b, the optimization curves for skin cancerous cell (Basal) and its corresponding normal cell are shown where the sensor depicts the peak losses of 644 dB/cm at 2322 nm and 725 dB/cm at 3009 nm when the sensing surface is submerged in a sample liquid of RI 1.38 and RI 1.36, respectively. Again, for cervical cancerous cell (HeLa) and its corresponding normal cell, the optimization curves are shown in Figure 4c, where the peak losses are of 330 dB/cm at 1830 nm and 685 dB/cm at 2755 nm for RI of 1.392 and RI 1.368 successively. Finally, the adrenal glands cancerous cell (PC12) and its corresponding normal cell are optimized in Figure 4d, where the sensor shows the peak losses of 230 dB/cm at 1767 nm and 645 dB/cm at 2282 nm for the RI of 1.395 and RI 1.381 correspondingly. The maximum AS of Jurkat cell, Basal cell, HeLa cell, and PC12 cell with their corresponding normal cell are 147, 75, 100, and 200 RIU⁻¹ (highest one) at 2477, 3009, 2755, and 2282 nm gradually.

Figure 5a demonstrates the sensor resolutions and WS values as the function of RI. The sensor exhibits an excellent resolution of 2.37×10^{-6} RIU for RI 1.38 and the significantly intense WS of 42,145 nm/RIU (maximum WS), 34,350, 38,541, and 36,786 nm/RIU for Jurkat, Basal, HeLa, and PC12 cells concerning their corresponding normal cells, respectively. Although the sensitivity of a sensor gives an advanced idea about the quality and efficiency of its operation, in addition, several significant factors are highly recommended for optimizing a desired sensor, such as high FOM value (figure of merits), DL, SNR (signal-to-noise ratio) and R^2 value (should be very close to unity after polynomial fitting to be a very good sensor), etc. The ratio of spectral sensitivity for a specific RI and the corresponding full-width-half-maxima (FWHM), $\Delta \lambda_{1/2}$ defines the FOM of the sensor in that RI [48]. The SNR is the ratio of $\Delta \lambda_{\text{peak}}$ to the FWHM of the sensor [49] and the DL [50], which is the quotient of minimum resolution (R_{min}) and WS. The equations are as follows:

$$\text{FOM} = \frac{S_\lambda}{\Delta \lambda_{1/2}}, \quad (9)$$

$$\text{SNR} = \frac{\Delta \lambda_{\text{peak}}}{\Delta \lambda_{1/2}}, \quad (10)$$

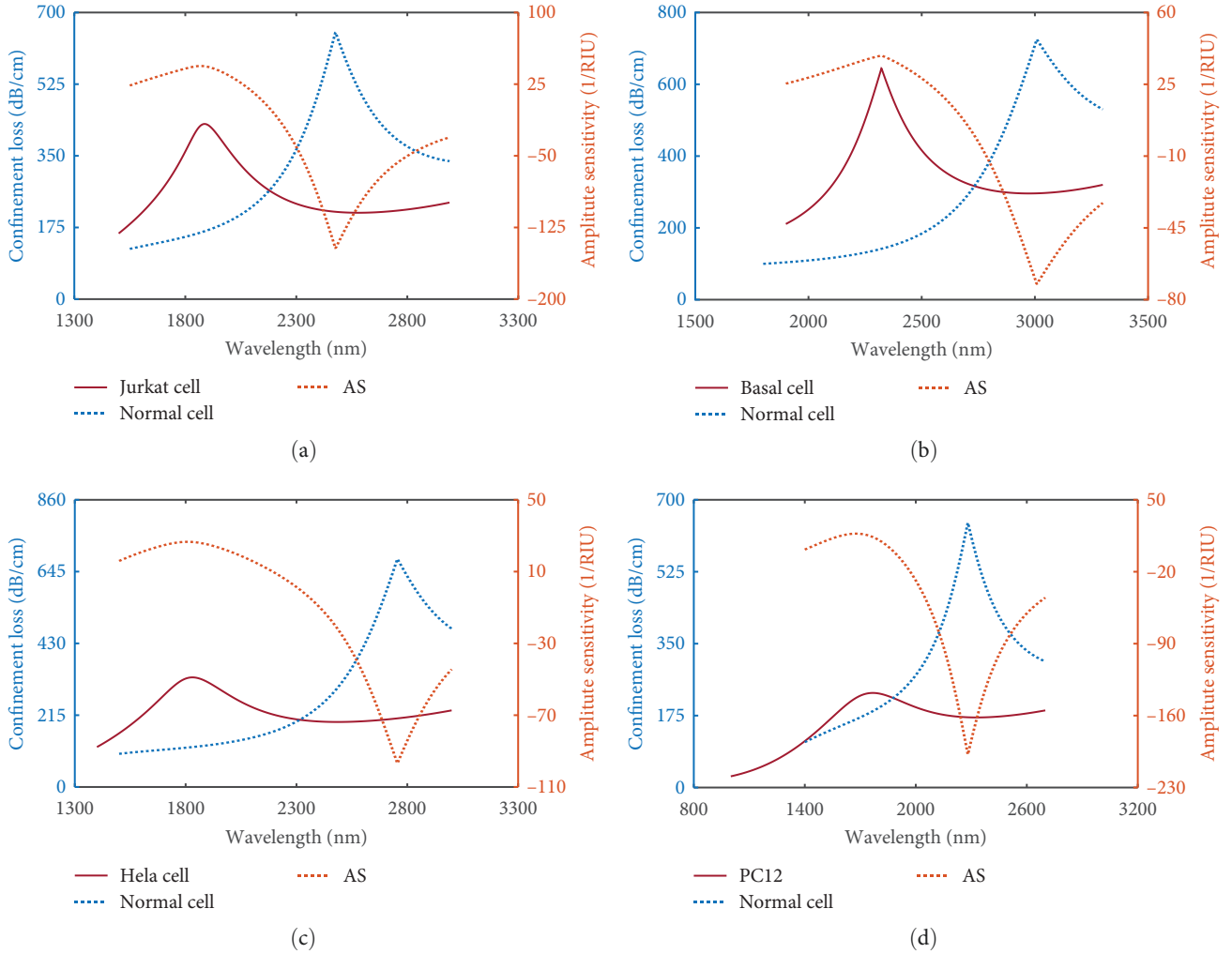


FIGURE 4: Loss spectrum and AS spectrum for optimization of (a) Jurkat cell, (b) Basal cell, (c) HeLa cell, and (d) PC12 with their corresponding normal cell. AS, amplitude sensitivity.

$$DL = \frac{R_{\min}}{S_{\lambda}}. \quad (11)$$

Figure 5b shows the graphs of DL and SNR values of the proposed model. The highest DL and SNR are 7.0×10^{-11} RIU²/nm and 1.15, respectively; both are found at the RI of 1.38. In Figure 5c, the FOM and FWHM curves are displayed, where FOM signifies the output efficiency of a sensor. The sensor illustrates the maximum value of FOM is 58 RIU⁻¹ for RI 1.38. The maximum and minimum values of FWHM are 1545 and 598 nm at RI of 1.395 and 1.38, respectively. Finally, Figure 5d illustrates the 2nd-order polynomial fitting curve, where the sensor gives the R^2 value of 0.9966, which is extremely close to the unity, indicating that the proposed model is highly responsive [35]. Table 2 displays the outcomes of the proposed sensor, where we have also evaluated the wavelength shift differences between each type of cancerous cell and their corresponding normal cell that is introduced to avoid the effect of concentration of different samples on the SPR resonance shift [51]. However, it is evident from the above discussion that our proposed SPR model

is outstanding for cancer detection because of its noticeably large values of resonant shift.

4. Optimization and Fabrication Tolerance

To get the finest efficiency and identify any possible imperfections of tolerable fabrication, we thoroughly analyzed several slightly different models from the proposed one and did the optimality investigations of each kind of structural variable to fix the perfect one. We have taken into account modal loss variations mostly to accomplish this critical study (as we stated before propagation loss is directly connected with sensor sensitivity) besides AS and WS in some cases for more clarities. We did all simulations for the Jurkat cell (1.39) and its corresponding normal cell (1.376).

Figure 6 represents the investigations of fiber core engineering. Initially, we investigated a solid-core type structure where the AH at the center point (Figure 6a) has been omitted and got almost similar values to the proposed one in terms of peak losses and AS, which are of 447 dB/cm, 667 dB/cm, and 148 RIU⁻¹, but a lower WS of 36,571 nm/RIU. Later, in Figure 6b, we erased the two SCD AH at the bottom portion

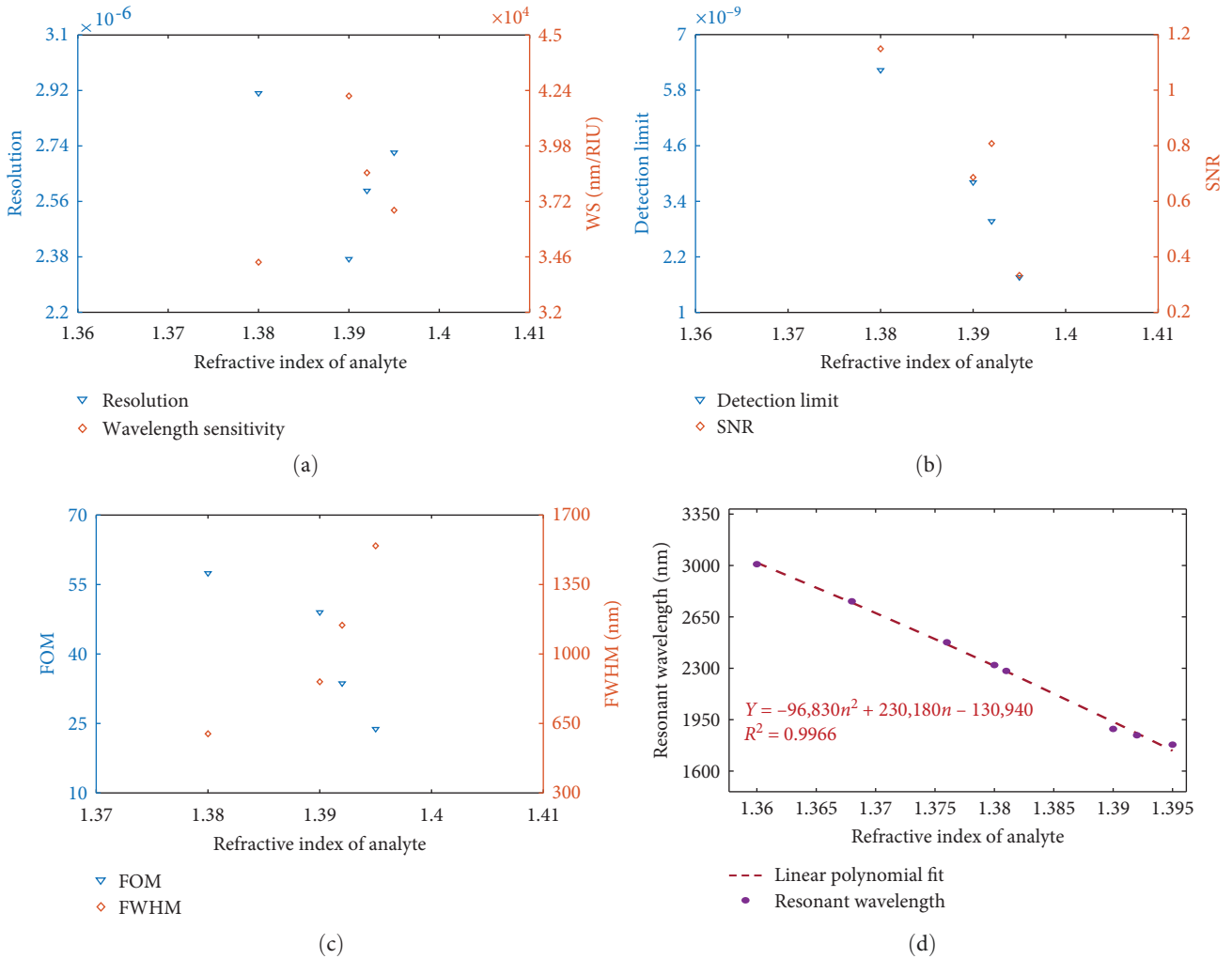


FIGURE 5: (a) Resolution and WS [47] curves, (b) DL and SNR curves, (c) FOM and FWHM, and (d) 2nd order polynomial fitting curve for optimized cancerous cells and their corresponding normal cells. DL, detection limit; FWHM, full-width-half-maxima; SNR, signal-to-noise ratio; WS, wavelength sensitivity.

of the proposed structure that exhibits lower AS and WS of only 13 RIU^{-1} and $11,500 \text{ nm/RIU}$ but higher peak losses of 803 and 680 dB/cm than the proposed values. Figure 6c portrays a reverse core where a small SCD AH is placed at the center surrounded by the six smaller SCD AH. However, in this case, the sensor also gives very subordinate sensitivity outcomes to the optimized one (maximum AS and WS are 18 RIU^{-1} and $12,142 \text{ nm/RIU}$, and the peak losses are 708 dB/cm, 610 dB/cm correspondingly). Lastly, three small SCD AH are kept in series centrally (Figure 6d), and consequently, the sensor displays moderate peak losses and lower spectral sensitivity performance than the optimized one but the lowest AS (Table 3). However, from the above analysis, we can easily understand the precision of using the proposed method. Table 3 illustrates the optimization table of fiber core engineering.

Figure 7 depicts the comparative propagation loss and AS curves of blood cancer cells and their corresponding normal cell (RI of 1.39 and 1.376 successively) regarding different types of plasmonic materials. It provides clarity about why

we have chosen Ti as a plasmonic material in our proposed PCF sensor. However, Figure 7a is illustrated for graphene, which exhibits resonant propagation losses of 461 and 660 dB/cm correspondingly. The WS and AS are $37,928 \text{ nm/RIU}$ and 149 RIU^{-1} successively. Similarly, Figure 7b shows the plots for indium-tin-oxide (ITO), which depicts the peak confinement losses of 52 and 48 dB/cm correspondingly, and the wavelength and AS for ITO are 2857 nm/RIU and 189 RIU^{-1} successively. Finally, Figure 7c shows the curves of Ti (our proposed plasmonic material), which displays the peak confinement losses for RI 1.39 and 1.376 are 427 and 651 dB/cm correspondingly. The WS and AS are $42,145 \text{ nm/RIU}$ and 147 RIU^{-1} successively. Finally, from Figure 7d, it is evident that there are slight differences among peak AS of the three plasmonic materials, although the wavelength sensitivities depict a dramatic change, and the highest value ($42,145 \text{ nm/RIU}$) was found for the Ti. Though the lowest losses were found for the ITO, the WS for ITO is very much less than others. In this case, a comparison is made between graphene and Ti; only the AS of graphene is slightly higher than Ti, which is

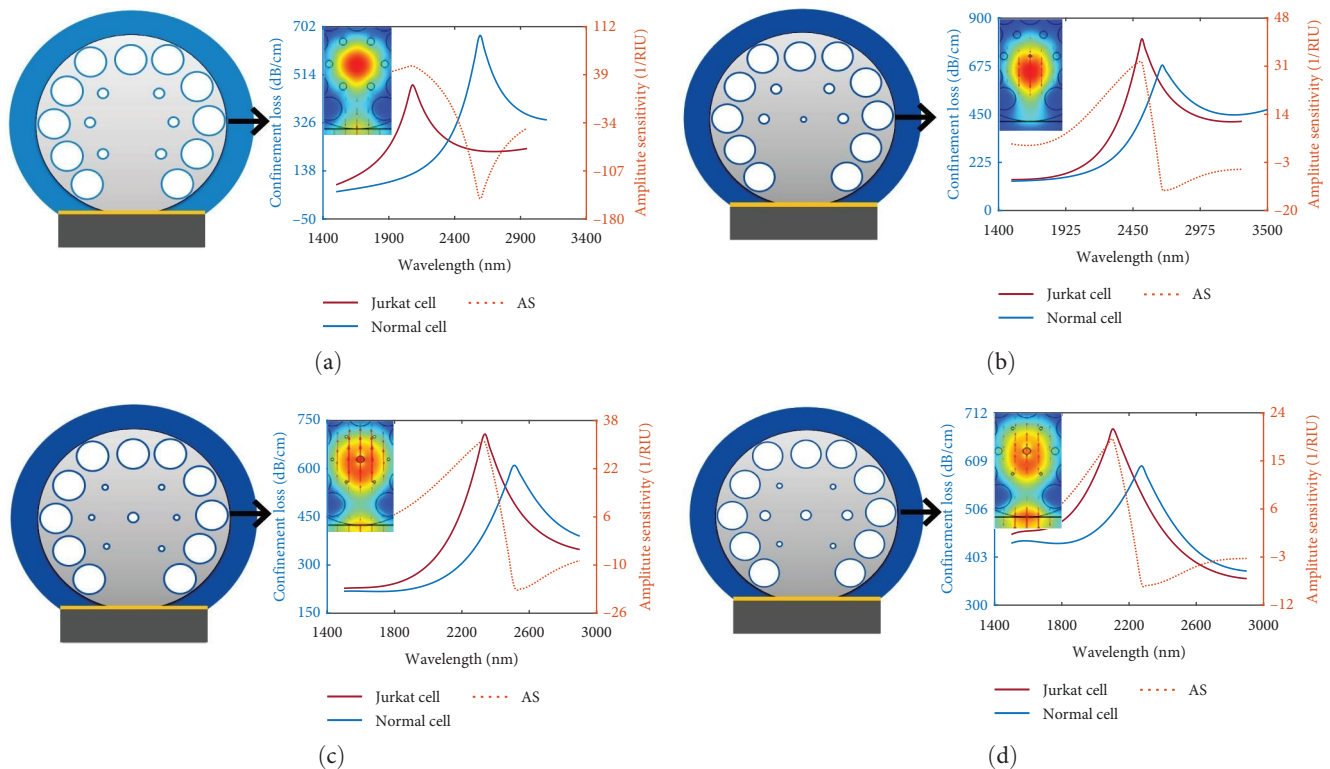


FIGURE 6: The impact of different types of AHs (those are SCD) in the distribution of light and propagation loss with field ordination of core-mode while the channels are filled with liquid RI of 1.39 and 1.376. (a) The smallest SCD AH in the center is excluded, (b) two small SCD AHs are excluded those are closer to the flat side, (c) rearranging the smallest and small SCD AHs reversely, and (d) placing three small AHs in series. AH, air hole; AS, amplitude sensitivity; RI, refractive index; scaled-downSCD, scaled-down.

almost avoidable, but the values of the other two parameters (WS and peak loss) for Ti are better than the graphene. Therefore, Ti is the most precise plasmonic material among the three optimized plasmonic materials for our presented sensor.

Similarly, to find the best sensing outcomes, optimizations of the parameters are highly required and our presented sensor shows indicatory changes while we executed the optimization of the dimensional parameter for the RIs of 1.39 and 1.376. Although the plasma frequency of a component is only related to the relative permittivity of the material, the effective RI concentration is greatly affected by the thickness of the metallic film [52]. Furthermore, the performance of the sensor effectively relies on the change of Ti layer thickness because surface plasmon waves are produced at the metal layer. Due to the damp effect, the depth of loss is changed as the thickness of the metal layer variation [39]. Thus, the effect of the changes in the metal layer thickness is portrayed in Figure 8, which shows the confinement losses, AS, and WS curves for the variation of the Ti layer from 35 to 45 nm.

In Figure 8a, at $t=35$ nm, the sensor displayed peak confinement losses of 595 and 681 dB/cm, which are 39% and 5% higher than the values for the proposed thickness. Consequently, the maximum AS and WS are 191 RIU^{-1} (30% higher) and $37,642 \text{ nm/RIU}$ (10.7% less), respectively. Similarly, at 45 nm thickness, the maximum propagation loss depths of 235 and 693 dB/cm are found, respectively, which

are -45% and $+6.5\%$ of the desired values. Although the propagation loss for the RI 1.39 is much less than the desired value, the maximum AS and WS are lower than the proposed thickness ($t=45$ nm), which are 132 RIU^{-1} (-10.2% of 147 RIU^{-1}) and $32,714 \text{ nm/RIU}$ (-22.3% of $42,145 \text{ nm/RIU}$) successively. The comparative AS and WS curves for different plasmonic material thicknesses are depicted in Figure 8b,c, respectively. However, at the thickness of 40 nm, we got moderate peak losses and AS besides the highest WS values (best phase shifting). Therefore, we chose the 40 nm thickness as the optimum Ti layer.

In the rest of the figures, the optimization tolerance has been taken into account to maximize the functional efficiency, and the investigation has been conducted over $\pm 10\%$ variations of the structural parameter's optimum values for the Jurkat cell. Figure 9a,c, and e shows the transmission loss as the function of the optimization of three different AHDs (thinner, thin, and large) that exhibit the resonant wavelength dislocations of 33, 163, and 117 nm for the worst case successively. Furthermore, it also obvious that loss curves increased gradually with the decrement of the AHD of thinner AH (447 dB/cm for -10% and 410 dB/cm for $+10\%$), thin AH (667 dB/cm for -10% and 272 dB/cm for $+10\%$), and thick AH (443 dB/cm for -5% and 308 dB/cm for $+10\%$). But, for the optimum values of the three AHDs, we got either moderate (only except for thinner AHD, for -10% , though the sensor exhibits slightly higher WS, loss is also highest in this case) or finest WS values that were measured by taking into

TABLE 3: Fiber core optimization table.

Fiber core	Resonant wavelength (nm)	Peak loss (dB/cm)	AS (RIU ⁻¹)	WS (nm/RIU)
Solid	2080 (1.390)*	447	148	36,571
	2592 (1.376)**	667		
Omitted	2521 (1.390)	803	13	11,500
	2682 (1.376)	680		
Inverse	2338 (1.390)	708	18	12,142
	2508 (1.390)	610		
Series	2103 (1.390)	677	9	12,500
	2278 (1.390)	598		
Proposed	1887 (1.390)	427	147	42,145
	2477 (1.390)	651		

Abbreviations: AS, amplitude sensitivity; WS, wavelength sensitivity.

*Jurkat cell (RI = 1.390).

**Normal cell (RI = 1.376).

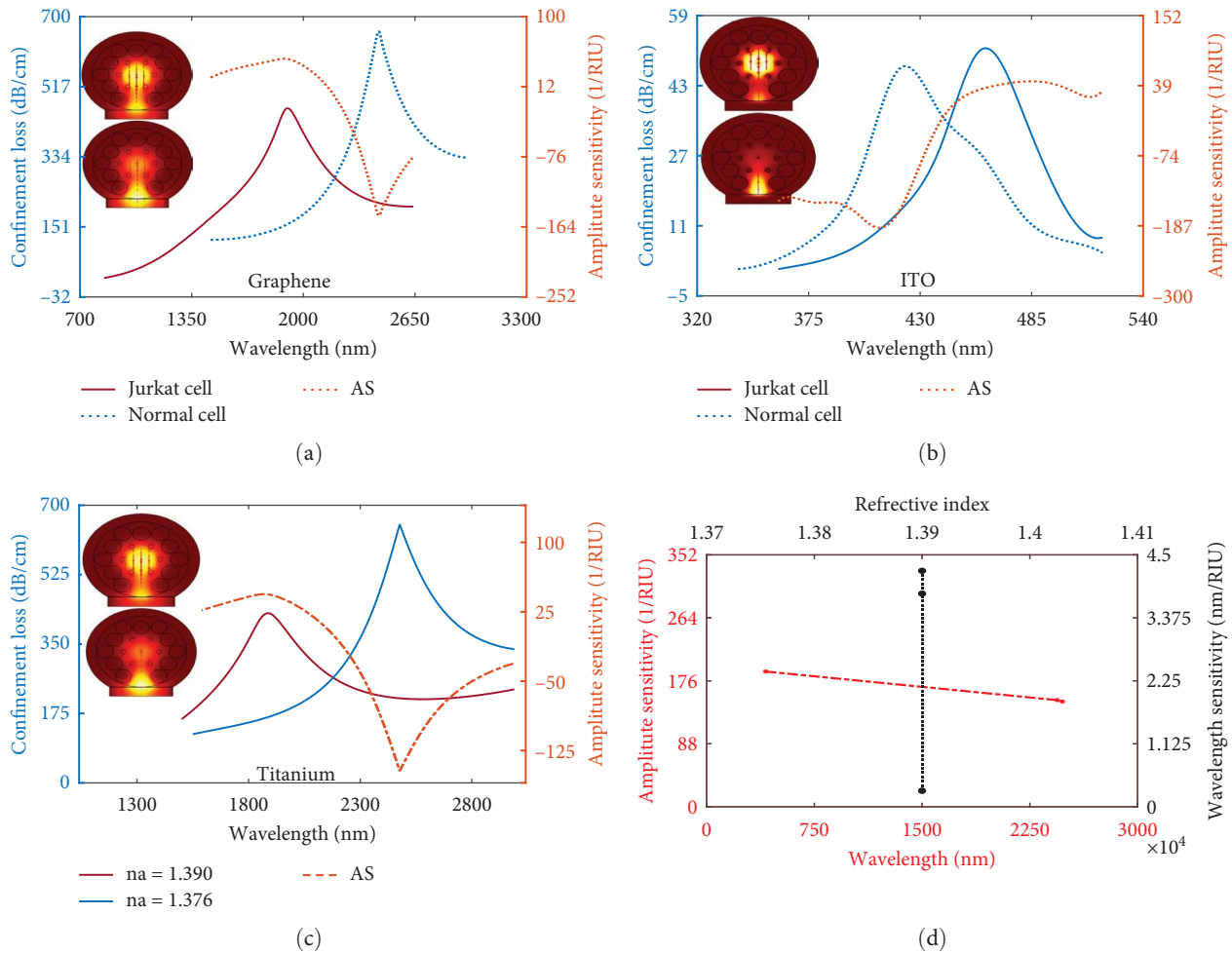


FIGURE 7: (a) Propagation loss and AS curve when the plasmonic materials are graphene, (b) ITO, (c) Ti, and (d) peak amplitude and WS curves for those afore-mentioned plasmonic materials. AS, amplitude sensitivity; ITO, indium-tin-oxide; Ti, titanium; WS, wavelength sensitivity.

account the Jurkat and its normal cell (Figure 9b,d,f). The above discussion indicates that the sensor displays the maximum performance at optimum values which also clarifies the precision of selecting the optimum values as the diameter of the three different AHs.

However, in Figure 10, the same fabrication tolerance process is investigated for the variations of the pitch value, PML, and AL, where the loss curves illustrate an increasing trend with the increment of the parameters in most cases except for the AL variations (displaying an irregular response).

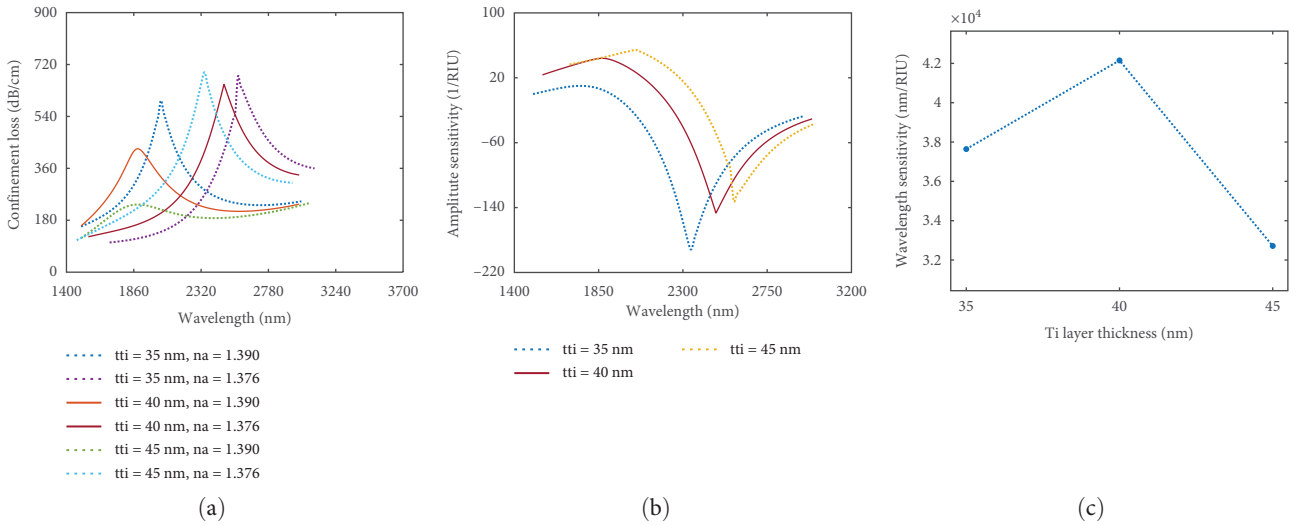


FIGURE 8: (a) Propagation loss spectrum, (b) AS curve, and (c) WS curve for varying Ti layer thickness for y -polarized mode. AS, amplitude sensitivity; Ti, titanium; WS, wavelength sensitivity.

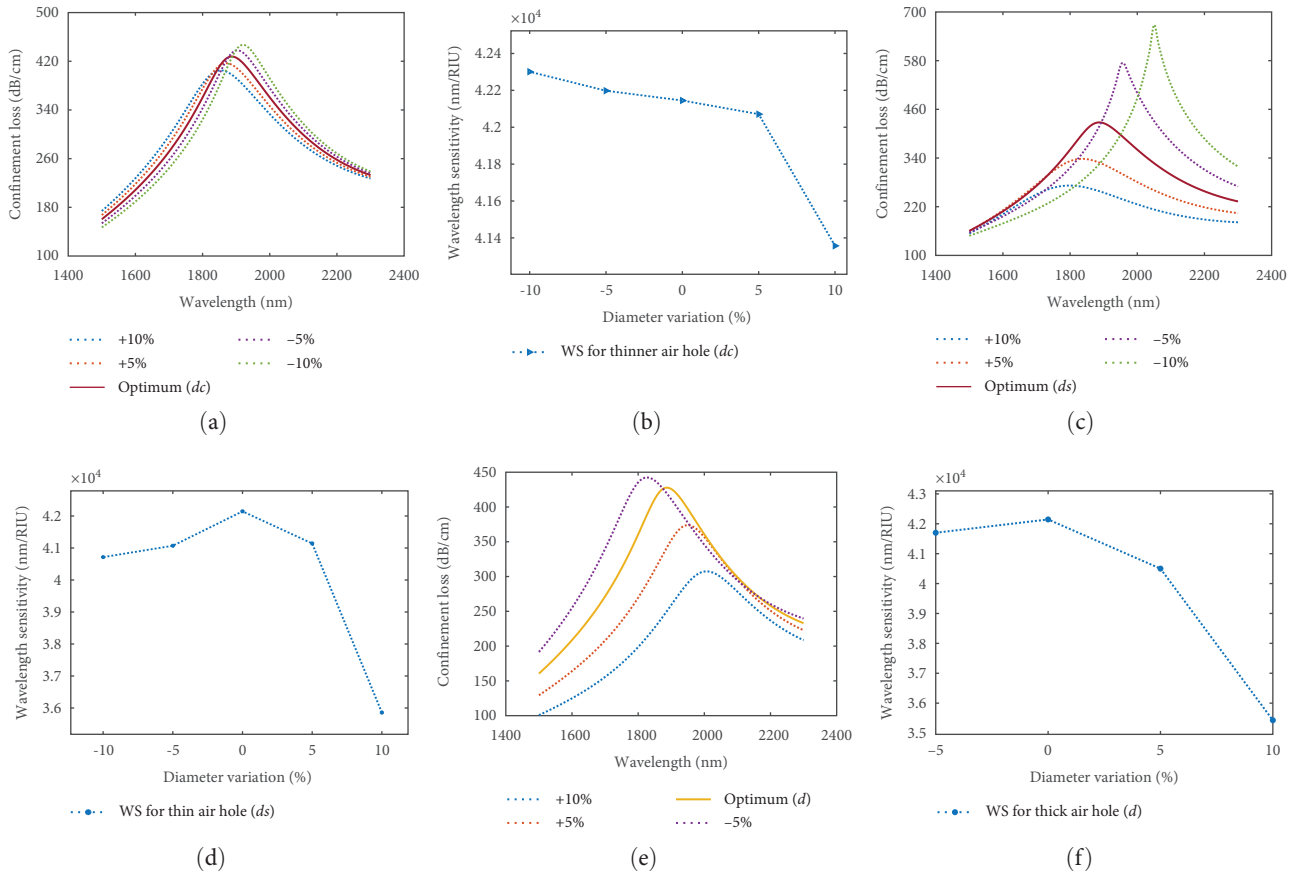


FIGURE 9: Transmission loss spectrums and its corresponding wavelength interrogation response for optimizing fabrication tolerance effect (a, b) for thinner AH's diameter variations, (c, d) for thin AH's diameter variations, and (e, f) for thick AH's diameter variations, respectively. AH, air hole.

Figure 10a demonstrates the corresponding transmission loss spectrums for the pitch size variations over $\pm 10\%$ of the optimum value, where it can be seen that a significantly large wavelength shifting (971 nm for +10%) can occur in the worst

case. This type of huge deviation means that our sensor is extremely sensitive to pitch value changes. Therefore, we must ensure a stable environment so that it cannot be affected though. Figure 10b demonstrates the superiority of the optimum value

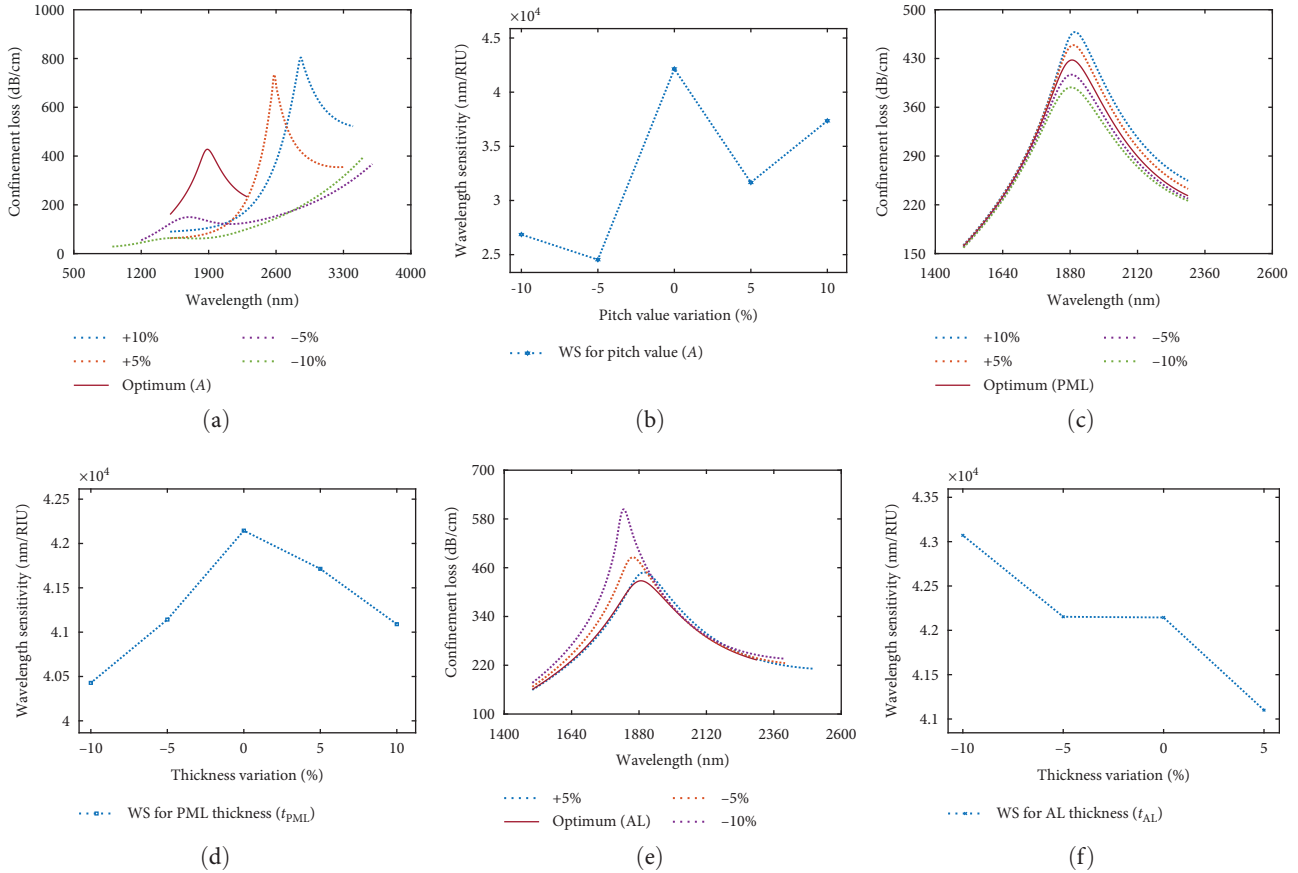


FIGURE 10: Transmission loss spectrums and its corresponding wavelength interrogation response for optimizing fabrication tolerance effect (a, b) for pitch value variations (c, d) for PML layer variations and (e, f) for AL variations, respectively. AL, analyte layer; PML, perfectly matched layer.

TABLE 4: The result parallelism table of the presented sensor with previously reported structures.

Ref.	Structure type	No. of simultaneous detections	RI range	Operating wavelength	Wavel. sens. (nm/RIU)	Ampl. sens. (RIU ⁻¹)	Wavel. resolution (RIU)
[35]	Dual polarized propagation controlled sensor	2	1.33–1.39	560–1250	13,700	852	7.30×10^{-6}
[53]	Cancer detection with SPR-PCF biosensor	1	1.392–1.401	560–1200	15,400	654	—
[54]	Cancer-detecting PCF-SPR biosensor with external sensing	1	1.36–1.401	600–1600	14,285	—	7.77×10^{-6}
[55]	Twin core PCF sensor for blood cancer detection	1	1.376–1.39	1400–1800	8571	—	—
[56]	Segmented Ag–TiO ₂ PCF-SPR sensor	1	1.33–1.36	500–850	10,600	633	9.43×10^{-6}
[36]	Ti-coated D-shaped PCF-SPR sensor	1	1.36–1.401	1150–2000	17,500	420	1.50×10^{-5}
[57]	D-shaped SPR-PCF sensor	1	1.33–1.38	10,493	10,493	N/A	9.50×10^{-6}
[37]	D-shaped polished RI sensor	1	1.37–1.41	N/A	6,000	N/A	1.70×10^{-5}
Proposed work	Ti-coated D-shaped extremely sensitive sensor	1	1.36–1.395	1000–3300	42,145	200	2.37×10^{-6}

Abbreviations: PCF, photonic crystal fiber; RI, refractive index; SPR, surface plasmon resonance; Ti, titanium.

over other changes in case of WS that truly helps us to select the optimum value as the pitch size for our proposed sensor, whereas the sensor depicts very low wavelength dislocations due to PML (10 nm for +10%) and AL (62 nm for –10%)

variations in the severe cases (Figure 10c,e) and the maximum and minimum propagation losses are 450 dB/cm (at +10%) and 385 dB/cm (at –10%) for PML changes and 604 dB/cm (at –10%) and 427 dB/cm (optimum value) for AL variations.

However, still, our proposed sensor is still showing either the best or moderate performance (for PML and AL variations) in the case of WS (Figure 10d,f). In summary, after thoroughly analyzing these previously discussed numerical investigations, the precision of choosing the optimum values as our proposed sensor's parameters can be easily understood. Table 4 presents the comparison of the proposed sensor's performance alongside previously reported designs.

5. Conclusion

In this manuscript, the presented SPR sensor with blue shift characteristics is superior to other reported D-shape PCFs in terms of optical and sensing parameters. This SPR biosensor is numerically analyzed to perform highly sensitive detection characteristics based on external sensing method. FEM is used to conduct the investigation, which guarantees that the detection performance parameters are very promising. Excellent WS of almost 34,350, 36,786, 38,542, 42,143 nm/RIU for γ -polarization mode, and AS around -75 , -100 , -150 , -200 RIU $^{-1}$ for skin cancer, cervical cancer, adrenal glands cancer, and blood cancer, respectively. Moreover, the resolution level ranges from 2.37×10^{-6} to 3.00×10^{-6} RIU, and the highest DL is about 7.0×10^{-11} RIU $^{-2}$ /nm for skin cancer, cervical cancer, adrenal glands cancer, and blood cancer, respectively. Due to these attractive detection properties with highly sensitive characteristics, the proposed sensor would be an attractive addition to existing sensing technology for label-free biochemical sensing and could find potential application in any case related to early detection of cancer cells or microbial infections.

Data Availability Statement

The data presented in this study are available in the article.

Conflicts of Interest

The authors declare no conflicts of interest.

Funding

The work did not receive any funding. However, the authors sincerely acknowledge the support from the Rajshahi University of Engineering and Technology. The funder was not involved in the manuscript writing, editing approval or decision to publish.

References

- [1] Cancer, 2022, <https://www.who.int/news-room/fact-sheets/detail/cancer>, [Online]. Available.
- [2] R. Singh, "Nanotechnology Based Therapeutic Application in Cancer Diagnosis and Therapy," *3 Biotech* 9 (2019): 415.
- [3] H. Sung, J. Ferlay, R. L. Siegel, et al., "Global Cancer Statistics 2020: GLOBOCAN Estimates of Incidence and Mortality Worldwide for 36 Cancers in 185 Countries," *CA: A Cancer Journal for Clinicians* 71, no. 3 (2021): 209–249.
- [4] P. Sharma, P. Sharan, and P. Deshmukh, "A Photonic Crystal Sensor for Analysis and Detection of Cancer Cells," in *2015 International Conference on Pervasive Computing (ICPC)*, (IEEE).
- [5] F. Haider, M. Mashrafi, R. Haider, R. A. Aoni, R. Ahmed, and R. Ahmed, "Asymmetric Core-Guided Polarization-Dependent Plasmonic Biosensor," *Applied Optics* 59, no. 26 (2020): 7829–7835.
- [6] A. A. Rifat, R. Ahmed, A. K. Yetisen, et al., "Photonic Crystal Fiber Based Plasmonic Sensors," *Sensors and Actuators B: Chemical* 243 (2017): 311–325.
- [7] S. Jiao, S. Gu, H. Fang, and H. Yang, "Analysis of Dual-Core Photonic Crystal Fiber Based on Surface Plasmon Resonance Sensor With Segmented Silver Film," *Plasmonics* 14, no. 3 (2019): 685–693.
- [8] F. Haider, R. A. Aoni, R. Ahmed, W. J. Chew, and G. A. Mahdiraji, "Alphabetic-Core Assisted Microstructure Fiber Based Plasmonic Biosensor," *Plasmonics* 15, no. 6 (2020): 1949–1958.
- [9] N. Jahan, M. M. Rahman, M. Ahsan, et al., "Photonic Crystal Fiber Based Biosensor for Pseudomonas Bacteria Detection: A Simulation Study," *IEEE Access* 9 (2021): 42206–42215.
- [10] L. Hajba and A. Guttman, "Circulating Tumor-Cell Detection and Capture Using Microfluidic Devices," *TrAC Trends in Analytical Chemistry* 59 (2014): 9–16.
- [11] T. Li, Q. Fan, T. Liu, X. Zhu, J. Zhao, and G. Li, "Detection of Breast Cancer Cells Specially and Accurately By An Electrochemical Method," *Biosensors and Bioelectronics* 25, no. 12 (2010): 2686–2689.
- [12] F.-R. Li, Q. Li, H.-X. Zhou, H. Qi, and C.-Y. Deng, "Detection of Circulating Tumor Cells in Breast Cancer With a Refined Immunomagnetic Nanoparticle Enriched Assay and Nested-RT-PCR," *Nanomedicine: Nanotechnology, Biology and Medicine* 9, no. 7 (2013): 1106–1113.
- [13] T. D. Bradley, Y. Wang, M. Alharbi, et al., "Optical Properties of Low Loss (70dB/km) Hypocycloid-Core Kagome Hollow Core Photonic Crystal Fiber for Rb and Cs Based Optical Applications," *Journal of Lightwave Technology* 31, no. 16 (2013): 3052–3055.
- [14] L. C. Clark Jr., "Implantable Gas-Containing Biosensor and Method for Measuring An Analyte Such As Glucose," Google Patents, 1988.
- [15] A. N. Yaroslavsky, R. Patel, E. Salomatina, et al., "High-Contrast Mapping of Basal Cell Carcinomas," *Optics Letters* 37, no. 4 (2012): 644–646.
- [16] J. Villatoro, V. Finazzi, V. P. Minkovich, V. Pruneri, and G. Badenes, "Temperature-Insensitive Photonic Crystal Fiber Interferometer for Absolute Strain Sensing," *Applied Physics Letters* 91, no. 9 (2007): 091109.
- [17] J. Zhou, Y. Zheng, J. Liu, X. Bing, J. Hua, and H. Zhang, "A Paper-Based Detection Method of Cancer Cells Using the Photo-Thermal Effect of Nanocomposite," *Journal of Pharmaceutical and Biomedical Analysis* 117 (2016): 333–337.
- [18] N. Nallusamy, R. V. J. Raja, and G. Joshva Raj, "Highly Sensitive Nonlinear Temperature Sensor Based on Modulation Instability Technique in Liquid Infiltrated Photonic Crystal Fiber," *IEEE Sensors Journal* 17, no. 12 (2017): 3720–3727.
- [19] Q. Wu, Y. Qu, J. Liu, et al., "Singlemode-Multimode-Singlemode Fiber Structures for Sensing Applications—A Review," *IEEE Sensors Journal* 21, no. 11 (2021): 12734–12751.
- [20] L. Chen, Y. K. Leng, B. Liu, et al., "Ultra-high-Sensitivity Label-Free Optical Fiber Biosensor Based on a Tapered Singlemode-no Core-Singlemode Coupler for *Staphylococcus aureus* Detection," *Sensors and Actuators B: Chemical* 320 (2020): 128283.

- [21] R. Kumar, Y. Leng, B. Liu, et al., "Ultrasensitive Biosensor Based on Magnetic Microspheres Enhanced Microfiber Interferometer, Biosens.," *Biosensors and Bioelectronics* 145 (2019): 111563.
- [22] N. H. Salah, A. Pal, and A. Uniyal, "Enhancing Precision in Fuel Adulteration Detection: Utilizing A Wavelength Interrogation Surface Plasmon Resonance Approach," *Plasmonics* (2024).
- [23] A. Bijalwan, A. Uniyal, R. B. Yadav, A. S. A. Alsubaie, K. H. Mahmoud, and A. Pal, "Enhanced Sensing: E7-Liquid Crystal-Based Surface Plasmon Temperature Sensor With Angle Interrogation," *Plasmonics* (2024).
- [24] A. H. Almwagani, A. Uniyal, P. Sarkar, et al., "Magnesium Oxide and Silicon-Assisted Surface Plasmon Resonance Sensor for Gas Detection: A Performance Analysis," *Plasmonics* (2024).
- [25] D. Pal, A. H. Almwagani, S. Das, et al., "A Highly Sensitive Long-Range Surface Plasmon Resonance Biosensor for the Determination of Hemoglobin Content in Human Blood," *Plasmonics* (2024).
- [26] B. Karki, Y. Trabelsi, P. Sarkar, A. Pal, and A. Uniyal, "Tuning Sensitivity of Surface Plasmon Resonance Gas Sensor Based on Multilayer Black Phosphorous," *Modern Physics Letters B* (2024): 2450364.
- [27] H. Kumar B. M., A. M. Vaibav, and P. C. Srikanth, "2D Photonic Crystal Based Biosensor for Detection of Cervical Cancer Cell," in *2020 IEEE International Conference on Electronics, Computing and Communication Technologies (CONECCT)*, (IEEE, 2020).
- [28] B. Karki, P. Sarkar, G. Dhiman, G. Srivastava, and M. Kumar, "Platinum Diselenide and Graphene-Based Refractive Index Sensor for Cancer Detection," *Plasmonics* 19, no. 2 (2024): 953–962.
- [29] B. Karki, A. Uniyal, A. Pal, and V. Srivastava, "Advances in Surface Plasmon Resonance-Based Biosensor Technologies for Cancer Cell Detection," *International Journal of Optics* 2022 (2022): 1476254.
- [30] B. Karki, Y. Trabelsi, A. Uniyal, and A. Pal, "Zinc Sulfide, Silicon Dioxide, and Black Phosphorus Based Ultra-Sensitive Surface Plasmon Biosensor," *Optical and Quantum Electronics* 54, no. 2 (2022): 107.
- [31] B. Karki, A. Pal, P. Sarkar, R. B. Yadav, A. Muduli, and Y. Trabelsi, "ZnO-Silicon Enhanced Surface Plasmon Resonance Sensor for Chemical Sensing," *Silicon* 16, no. 9 (2024): 3861–3872.
- [32] B. Karki, Y. Trabelsi, A. Uniyal, A. Pal, and R. B. Yadav, "Detection of Fat Concentration Milk Using TMDc-Based Surface Plasmon Resonance Sensor," *Modern Physics Letters B* (2024): 2450253.
- [33] B. Karki, A. Pal, P. Sarkar, A. Uniyal, and R. B. Yadav, "Gold, MXene, and Graphene Nanofilm-Based Surface Plasmon Resonance Sensor for Malaria Detection," *Journal of Optics* (2024).
- [34] B. Karki, A. Uniyal, P. Sarkar, A. Pal, and R. B. Yadav, "Sensitivity Improvement of Surface Plasmon Resonance Sensor for Glucose Detection in Urine Samples Using Heterogeneous Layers: An Analytical Perspective," *Journal of Optics* (2023): 1–11.
- [35] A. M. T. Hoque, A. Islam, F. Haider, H. A. Bin Abdul Rashid, R. Ahmed, and R. A. Aoni, "Dual Polarized Surface Plasmon Resonance Refractive Index Sensor Via Decentering Propagation-Controlled Core Sensor," *Optics Continuum* 1, no. 7 (2022): 1474.
- [36] M. A. Jabin, K. Ahmed, M. J. Rana, et al., "Surface Plasmon Resonance Based Titanium Coated Biosensor for Cancer Cell Detection," *IEEE Photonics Journal* 11, no. 4 (2019): 1–10.
- [37] H. Liang, T. Shen, Y. Feng, H. Liu, and W. Han, "A D-Shaped Photonic Crystal Fiber Refractive Index Sensor Coated With Graphene and Zinc Oxide," *Sensors* 21, no. 1 (2021): 71.
- [38] L. Skowronski, "Optical Properties of Titanium in the Regime of the Limited Light Penetration," *Materials* 13, no. 4 (2020): 952.
- [39] M. R. Hasan, S. Akter, A. A. Rifat, et al., "Spiral Photonic Crystal Fiber-Based Dual-Polarized Surface Plasmon Resonance Biosensor," *IEEE Sensors Journal* 18, no. 1 (2018): 133–140.
- [40] N. Ayyanar, G. T. Raja, M. Sharma, and D. S. Kumar, "Photonic Crystal Fiber-Based Refractive Index Sensor for Early Detection of Cancer," *IEEE Sensors Journal* 18, no. 17 (2018): 7093–7099.
- [41] A. M. T. Hoque, K. F. Al-Tabatabaie, M. E. Ali, A. M. Butt, S. S. I. Mitu, and K. K. Qureshi, "U-Grooved Selectively Coated and Highly Sensitive PCF-SPR Sensor for Broad Range Analyte RI Detection," *IEEE Access* 11 (2023): 74486–74499.
- [42] H. N. Rafi, M. R. Kaysir, and M. J. Islam, "Air-Hole Attributed Performance of Photonic Crystal Fiber-Based SPR Sensors," *Sensing and Bio-Sensing Research* 29 (2020): 100364.
- [43] Q. M. Kamrunnahar, J. R. Mou, and M. Momtaj, "Dual-Core Gold Coated Photonic Crystal Fiber Plasmonic Sensor: Design and Analysis," *Results in Physics* 18 (2020): 103319.
- [44] M. R. Islam, M. A. Jamil, M. S. U. Zaman, et al., "Design and Analysis of Birefringent SPR Based PCF Biosensor With Ultra-High Sensitivity and Low Loss," *Optik* 221 (2020): 165311.
- [45] P. Sharan, S. M. Bharadwaj, F. D. Gudagunti, and P. Deshmukh, "Design and Modelling of Photonic Sensor for Cancer Cell Detection," in *2014 International Conference on the IMPact of E-Technology on US (IMPETUS)*, (IEEE).
- [46] R. C. Jorgenson and S. S. Yee, "A Fiber-Optic Chemical Sensor Based on Surface Plasmon Resonance," *Sensors and Actuators B: Chemical* 12, no. 3 (1993): 213–220.
- [47] D. Vijayalakshmi, C. T. Manimegalai, N. Ayyanar, D. Vigneswaran, and K. Kalimuthu, "Detection of Blood Glucose With Hemoglobin Content Using Compact Photonic Crystal Fiber," *IEEE Transactions on NanoBioscience* 20, no. 4 (2021): 436–443.
- [48] S. M. A. S. Sunny, T. Ahmed, S. M. Hiam, and A. K. Paul, "Highly Sensitive Externally Metal Coated Plasmonic Refractive Index Sensor Based on Photonic Crystal Fiber," *Optik* 243 (2021): 167482.
- [49] F. Haider, R. A. Aoni, R. Ahmed, W. J. Chew, and G. A. Mahdiraji, "Plasmonic Micro-Channel Based Highly Sensitive Biosensor in Visible to mid-IR," *Optics & Laser Technology* 140 (2021): 107020.
- [50] M. M. Rahman, M. A. Molla, A. K. Paul, M. A. Based, M. M. Rana, and M. S. Anower, "Numerical Investigation of a Highly Sensitive Plasmonic Refractive Index Sensor Utilizing Hexagonal Lattice of Photonic Crystal Fiber," *Results in Physics* 18 (2020): 103313.
- [51] W. Wang, Z. Mai, Y. Chen, et al., "A Label-Free Fiber Optic SPR Biosensor for Specific Detection of C-Reactive Protein," *Scientific Reports* 7, no. 1 (2017): 1–8.
- [52] M. Moznuzzaman, M. R. Islam, and I. Khan, "Effect of Layer Thickness Variation on Sensitivity: An SPR Based Sensor for Formalin Detection," *Sensing and Bio-Sensing Research* 32 (2021): 100419.
- [53] A. Yasli, "Cancer Detection With Surface Plasmon Resonance-Based Photonic Crystal Fiber Biosensor," *Plasmonics* 16, no. 5 (2021): 1605–1612.

- [54] A. Ramola, A. Marwaha, and S. Singh, "Design and Investigation of a Dedicated PCF SPR Biosensor for CANCER Exposure Employing External Sensing," *Applied Physics A* 127 (2021): 643.
- [55] M. A. Mollah, M. Yousufali, I. M. Ankan, M. M. Rahman, H. Sarker, and K. Chakrabarti, "Twin Core Photonic Crystal Fiber Refractive Index Sensor for Early Detection of Blood Cancer," *Sensing and Bio-Sensing Research* 29 (2020): 100344.
- [56] H. Fang, C. Wei, D. Wang, et al., "Research on Photonic Crystal Fiber Based on a Surface Plasmon Resonance Sensor With Segmented Silver-Titanium Dioxide Film," *Journal of the Optical Society of America B* 37, no. 3 (2020): 736–744.
- [57] G. An, X. Hao, S. Li, X. Yan, and X. Zhang, "D-Shaped Photonic Crystal Fiber Refractive Index Sensor Based on Surface Plasmon Resonance, Appl," *Applied Optics* 56, no. 24 (2017): 6988–6992.